Long-range magnetic interactions in Nd_2PdSi_3 and the formation of skyrmion phases in centrosymmetric metals

Viviane Peçanha-Antonio,[1,2,*] Zhaoyang Shan,[3] Michael Smidman,[3] Juba Bouaziz,[4] Bachir Ouladdiaf,[5] Iurii Kibalin,[5] Marie-Hélène Lemée-Cailleau,[5] Christian Balz,[2] Jakob Lass,[6] Daniel A. Mayoh,[7] Geetha Balakrishnan,[7] Julie B. Staunton,[7] Devashibhai Adroja,[2,8] and Andrew T. Boothroyd[1,†]

[1]*Department of Physics, University of Oxford, Clarendon Laboratory, Oxford OX1 3PU, United Kingdom*
[2]*ISIS Neutron and Muon Source, STFC Rutherford Appleton Laboratory, Didcot OX11 0QX, United Kingdom*
[3]*Center for Correlated Matter and School of Physics, Zhejiang University, Hangzhou 310058, China*
[4]*Department of Physics, The University of Tokyo, Bunkyo-ku, Tokyo 113-0033, Japan*
[5]*Institut Laue-Langevin, 6 Rue Jules Horowitz, B.P. 156, 38042 Grenoble Cedx 9, France*
[6]*PSI Center for Neutron and Muon Sciences, 5232 Villigen PSI, Switzerland*
[7]*Department of Physics, University of Warwick, Coventry CV4 7AL, United Kingdom*
[8]*Highly Correlated Matter Research Group, Physics Department, University of Johannesburg, Auckland Park 2006, South Africa*

(Received 21 April 2025; revised 19 May 2026; accepted 10 June 2026; published 14 August 2026)

We present an extensive x-ray and neutron scattering study of the structure and magnetic excitations of Nd_2PdSi_3, a sister compound of Gd_2PdSi_3 that was recently found to host a skyrmion lattice phase despite its centrosymmetric crystal structure. Dispersive magnetic excitations were measured throughout the Brillouin zone and modeled to determine the magnetic interactions between Nd ions. Our analysis reveals that the magnetic interactions in this system extend over large distances and are significantly affected by a crystallographic superstructure formed by ordering of the Pd and Si atoms. The results suggest that the mechanism for the skyrmion phase formation in this family of materials, specifically Gd_2PdSi_3, is through the long-range Ruderman-Kittel-Kasuya-Yosida interactions rather than short-range triangular-lattice frustration.

DOI: 10.1103/vpy4-9zgh

I. INTRODUCTION

The discovery of magnetic skyrmions in noncentrosymmetric compounds with the B20 crystal structure [1–3] has revolutionized the study of spin topology in condensed matter. More than that, it has initiated a new field of research, *skyrmionics*, which aims to harness the exotic properties resulting from the coupling between magnetic and electronic degrees of freedom in these materials [4–6]. In proposals for a new generation of memory and logic devices based on skyrmion crystals (SkX), small skyrmion sizes, of the order of a few unit cells, are preferable over spin textures extending over large crystallographic scales [7–9]. Recent conceptual qubit constructions, for example, rely upon the information density a nanoscale SkX would be able to store [10,11].

Theoretical work has helped broaden the spectrum of candidate skyrmion crystals, to the extent that predictions for topologically nontrivial magnetism exist even for centrosymmetric compounds [12–21]. This is perhaps surprising given that the Dzyaloshinskii-Moriya interaction (DMI) usually responsible for stabilizing such phases is absent in crystals with inversion symmetry. In place of DMI a variety of different mechanisms have been proposed, some of which combine superexchange interactions with geometrical frustration [12–14,19] while others show that topological spin textures can be stabilized even in the absence of frustration or magnetic field [16,17,21]. Most theories involve exchange couplings of a long-range nature, requiring two or three nearest neighbors [12–17,20,21]. For metallic systems, the Ruderman-Kittel-Kasuya-Yosida (RKKY) type coupling, possibly in combination with magnetic field and weaker secondary interactions, provides a natural mechanism for the formation of skyrmionlike multi-**q** structures via Fermi-surface nesting [15,16,21–24]. Importantly, skyrmions in centrosymmetric materials are predicted to be much smaller and more densely packed than in noncentrosymmetric crystals.

Experiments have now confirmed the existence of a handful of such candidate centrosymmetric skyrmion compounds [25–29]. One of these is Gd_2PdSi_3, a member of a wider family of R_2PdSi_3 intermetallics with stacked triangular layers of R (rare-earth) atoms that have been extensively studied for their exotic magnetic properties [30–41]. Besides its anisotropic magnetic behavior and large negative magnetoresistance [41,42], Gd_2PdSi_3 was shown to host a skyrmion lattice phase in moderate applied magnetic fields [25]. The SkX was proposed to be a triple-**q** spin structure formed

*Contact author: viviane.antonio@stfc.ac.uk
†Contact author: andrew.boothroyd@physics.ox.ac.uk

Published by the American Physical Society under the terms of the Creative Commons Attribution 4.0 International license. Further distribution of this work must maintain attribution to the author(s) and the published article's title, journal citation, and DOI.

by the superposition of three spin helices at 120° to each other [25].

To understand the formation of a SkX in Gd_2PdSi_3 and other centrosymmetric metals, it is essential to quantify the magnetic interactions. This can be achieved via inelastic neutron scattering (INS) measurements of dispersive magnetic excitations, but for Gd_2PdSi_3 this is not straightforward. First, the magnetic order is complex. Second, the Pd and Si atoms form a superstructure that creates many inequivalent exchange paths. This superstructure lowers the hexagonal space group symmetry and has a significant influence on the electronic bands near the Fermi level [24], implying that any conduction-electron-mediated exchange must also be affected. Third, samples containing Gd are extremely challenging to study by INS owing to the large neutron absorption of Gd. The only neutron scattering studies reported so far used samples enriched with ^{160}Gd to reduce neutron absorption [43,44]. In Ref. [43], the authors analyzed INS and paramagnetic diffuse scattering data from a polycrystalline sample to develop a minimal model, and found evidence that the magnetic interactions extend beyond the first few nearest neighbors.

In this work we take a different approach, choosing instead to study the related non-SkX compound Nd_2PdSi_3, whose ferromagnetic structure is amenable to analysis, and whose neutron absorption is sufficiently small that high-quality INS data could be obtained from a single-crystal sample. We determine the Pd/Si superstructure in Nd_2PdSi_3 and take it into account when modeling the magnetic spectrum. We find clear evidence that the interactions extend over long distances, switching from mainly ferromagnetic to antiferromagnetic coupling with increasing atomic separation. Assuming the magnetic interactions are qualitatively similar in the Nd and Gd compounds (see below), our results support the theory that the SkX in centrosymmetric Gd_2PdSi_3 is most probably stabilized by long-range RKKY interactions.

II. EXPERIMENTAL METHODS

A single crystal of Nd_2PdSi_3 was grown by the optical floating-zone method (see Ref. [45] for details). The grown crystal was in the form of a rod of approximate dimensions 5 mm (diameter) × 50 mm (length). Parts of the same rod were used for all the measurements in this work. X-ray single-crystal diffraction was carried out at room temperature on a SuperNova Agilent diffractometer equipped with a Mo source.

Magnetic susceptibility measurements were performed with a Quantum Design MPMS3 SQUID-VSM magnetometer. The same piece of crystal was used for the neutron diffraction and magnetometry measurements. Figure 1 shows susceptibility data for a magnetic field of 100 Oe applied along the crystallographic **c** axis. The onset of spontaneous magnetization in the sample takes place at $T_C \simeq 14$ K. This temperature is about 1.7 K lower than that reported for powder samples in Refs. [34,46].

Neutron diffraction measurements were performed on the four-circle diffractometer D10+ at the Institut Laue-Langevin. A single crystal of dimensions 2 mm × 1 mm × 2 mm was cut from the main rod and fixed on a standard aluminum mount that was installed in a four-circle cryostat.

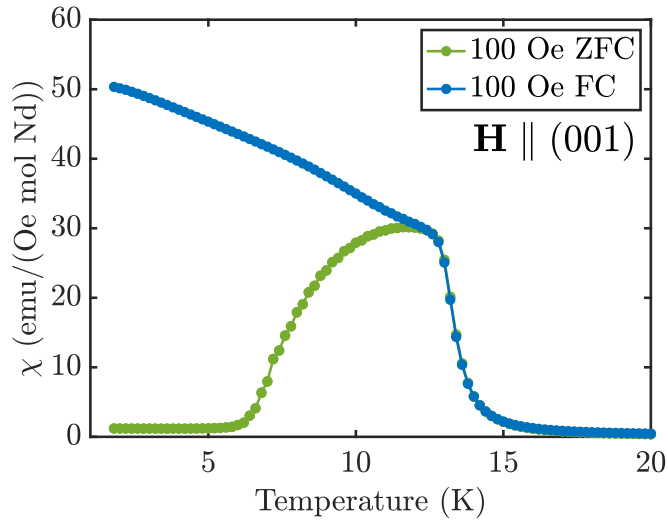


FIG. 1. Magnetic susceptibility measured on a single crystal of Nd_2PdSi_3 with $\mathbf{H} \parallel \mathbf{c}$. The sharp increase in susceptibility around 14 K marks the onset of ferromagnetism.

Neutrons of wavelengths $\lambda = 1.26$ and 2.36 Å were selected by Bragg diffraction from a Cu monochromator and a pyrolytic graphite monochromator, respectively. A graphite filter was used to suppress higher-order harmonic wavelengths in the incident beam. The scattered neutrons were recorded on a 94 × 94 mm^2 area detector. In the paramagnetic phase, a total of 740 inequivalent reflections were recorded using $\lambda = 1.26$ Å at a temperature of 150 K. Using $\lambda = 2.36$ Å, 111 inequivalent reflections were measured at 20 K, just above the phase transition temperature, and 94 at 2 K.

For the INS experiments, a sample of total mass around 5 g was fixed in an aluminum plate with the hexagonal [001] axis vertical. Time-of-flight INS was performed on the MERLIN and LET chopper spectrometers [47,48] at the ISIS Facility. On MERLIN, the experiment was divided into two parts making use of two different sample environments. In the first part, the sample was loaded in a closed-cycle refrigerator and data were recorded at 7.7 and 30 K. In the second, the sample was loaded in a helium cryostat and data were collected at 1.8 K. For both parts, the crystal was rotated through an angle of 125° in 1° steps around the vertical axis. The instrument chopper frequency was set at 250 Hz and operated in repetition-rate multiplication (RRM) mode, so that angular scans with incident energies E_i of 10, 20, and 53 meV were performed simultaneously.

On LET [48], the single crystal was fixed in an aluminum mount and loaded in a helium cryostat. During data collection, at a temperature of 1.8 K, the sample was rotated through an angle of 120° in 1° steps around the vertical axis. RRM enabled the simultaneous measurement of $E_i = 6$ and 15.6 meV, among other incident energies with less flux. For the former energy transfer, the FWHM of the energy resolution at the elastic line is 0.16 meV, down to about 0.06 meV at 5 meV.

Inelastic neutron scattering data in magnetic field were collected on the cold neutron multiplexing spectrometer CAMEA [49] at the Swiss Spallation Neutron Source at the Paul Scherrer Institut. For all magnetic fields, measurements were

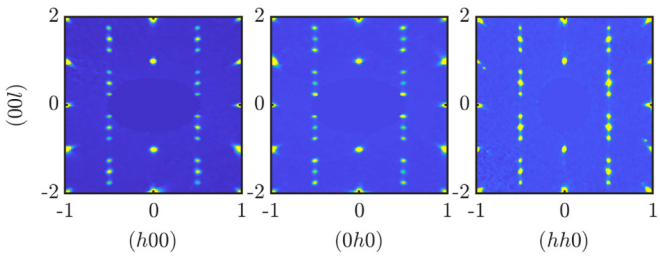


FIG. 2. x-ray diffraction in the $(h0l)$, $(0hl)$, and (hhl) reciprocal lattice planes, measured at room temperature.

performed with $E_i = 7$ and 8 meV (+0.13 meV for interlacing) and with the center of the detector tank at angles of $2\theta = -44°$ and $-48°$. In each case, the sample was rotated through an angle of 141° in 1° steps. For 0, 4, and 7 T also the elastic line was measured, i.e., $E_i = 5$ and 5.13 meV at $2\theta = -51°$ and $-56°$. In addition, at 0 and 7 T the spectrum was measured up to 11 meV with $E_i = 10$, 10.13, 12, 12.13, 14, 14.13 and $2\theta = -38°$ and $-42°$, covering 40° of sample rotation in steps of 1°. All points were measured with a monitor of 250 000 corresponding to ∼1 min at $E_i = 5$ meV and 2 min at $E_i = 14$ meV, except for the 0 T dataset, where a 190 000 monitor was used. Data were analyzed using the MJOLNIR software package [50].

III. CRYSTALLOGRAPHIC SUPERSTRUCTURE AND MAGNETIC ORDER

When first reported, the R_2PdSi_3 intermetallics were believed to adopt an AlB_2-type hexagonal structure with space group $P6/mmm$ [34]. In this description, $1a$ is the Wyckoff position of the R atoms, while the Pd/Si atoms randomly occupy the $2d$ sites. More recent single-crystal work demonstrated that Pd and Si in the heavy rare-earth members are in fact arranged in a $2a \times 2a \times 8c$ superstructure, where a and c are the hexagonal lattice parameters (see [51], and references therein).

Our single-crystal x-ray diffraction measurements, represented in Fig. 2, demonstrate that in Nd_2PdSi_3 the superstructure unit cell is enlarged by a factor $2a \times 2a \times 4c$ instead. Peaks are observed in the (hhl) reciprocal lattice plane at positions with $h = (2n + 1)/2$ and $l = m/4$, $l \neq$integer, where the indices h, k, and l refer to the parent hexagonal lattice and n, m are integers. The same conditions on h and l apply for the $(h0l)$ and $(0hl)$ reciprocal lattice planes.

The superstructure proposed in Ref. [51] is formed by the stacking of four layers in which the Pd atoms have distinct positions. These layers are labeled A, B, C, and D, and are shown in Fig. 3. In order to explain the extinction rules observed in their diffraction data, one of the assumptions made by the authors of Ref. [51] is that no two adjacent layers along the c axis are of the same type. Given that the periodicity of the unit cell in Nd_2PdSi_3 is increased along c by a factor of 4, the minimal unit cell that can be hypothesized in our case contains a vertical stacking of all four layers shown in Fig. 3.

Following symmetry considerations, it can be shown that six different twin domains contribute to the measured structure factors. These domains can be found by applying

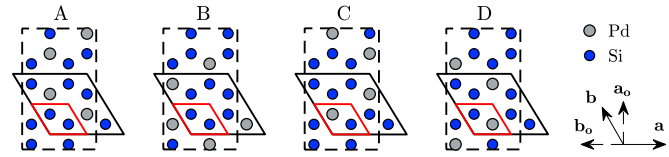


FIG. 3. Layers of ordered Pd and Si atoms in the superlattice ab plane of Nd_2PdSi_3. The four layers, labeled A, B, C, and D, are stacked along the **c** axis according to the sequences listed in Table I to form the different superstructure domains. Dashed and continuous black lines indicate the orthorhombic and hexagonal superstructure unit cells, respectively. The corresponding cell vectors are $\mathbf{a}_o$,$\mathbf{b}_o$ and **a**,**b**. The unit cell of the parent $P6/mmm$ space group is shown in red.

the symmetry operations $\{1, 3^-_{001}, 3^+_{001}, \bar{1}, \bar{3}^-_{001}, \bar{3}^+_{001}\}$ of the $P6/mmm$ space group to the stacking ABCD, which we refer to as *Domain 1*. The particular layer stacking of each domain is given in Table I. In Fig. 3, we reproduce the layers A, B, C, and D in the orthorhombic supercell, and show the relation between these lattice basis vectors with the hexagonal cell. Transformation matrices $\mathbf{T}_m$ relating the coordinates of domains $m = 2, 3, ..., 6$ with domain 1 in the $Fddd$ space group can be found in the Supplemental Material [52].

A. Structure refinement

The x-ray data measured at room temperature, and the neutron diffraction data measured in the paramagnetic phase at 150 K, were refined in the $Fddd$ group description using FULLPROF [53]. The model assumes an equal population of the six domains. Atomic positions of the general site $(32h)$ were not refined. In the reciprocal space maps shown in Fig. 2, a weak diffuse scattering can be observed along the $(00l)$ direction, evidencing that stacking faults occur. In order to (partially) account for that in the refinement of the peak intensities, the average occupation of Pd and Si sites was initially allowed to vary equally for all the domains, while the overall stoichiometry, i.e., three atoms of Si for each Pd, was kept constrained. Isotropic displacement parameters were refined at a later stage, during which the occupancies were kept constant at a value that gave the best agreement with the measured patterns.

TABLE I. The layer stacking of the six domains obtained by applying the symmetry operations $\{1, 3^-_{001}, 3^+_{001}, \bar{1}, \bar{3}^-_{001}, \bar{3}^+_{001}\}$ of the $P6/mmm$ space group to the ABCD sequence of planes. An alternative way of generating the six domains is considering all the possible ways of vertically stacking A, B, C, and D, requiring that no adjacent layer is the same and neglecting cyclic plane permutations, which are necessarily equivalent.

Domain	Stacking
1	ABCD
2	ADBC
3	ACDB
4	DCBA
5	CBDA
6	BDCA

TABLE II. Summary of the structural model assumed for the superstructure of Nd_2PdSi_3 in the space group $Fddd$. The atomic positions in the other five domains can be obtained with the transformation matrices $\mathbf{T}_m$ defined in the Supplemental Material [52].

Lattice parameters	$\mathbf{a}_o = 14.2402$ Å	$\mathbf{b}_o = 8.2216$ Å	$\mathbf{c}_o = 16.8595$ Å
Lattice angles	$\alpha = 90^\circ$	$\beta = 90^\circ$	$\gamma = 90^\circ$
Atom	Atomic position (Wyckoff site)	Occupancy	Isotropic displacement parameters (Å^2)
Nd	1/8,5/8,0 (16g)	0.5	0.52(3)
Nd	1/8,5/8,1/2 (16g)	0.5	0.52(3)
Pd/Si	7/24,1/8,1/8 (16e)	0.60(1)/0.4(1)	0.64(4)
Si/Pd	11/24,1/8,1/8 (16e)	0.866(1)/0.134(1)	0.64(4)
Si/Pd	13/24,7/8,1/8 (32h)	0.867(1)/0.133(1)	0.64(4)

A summary of the x-ray diffraction refinement results for Domain 1 is presented in Table II. A quantitative comparison between calculated and measured structure factors is shown in Figs. 4(a) and 4(b) for x-rays and neutrons, respectively.

B. Magnetic structure refinement

It was found in Ref. [46] that, in the magnetic long-range ordered phase, magnetic scattering is detected in integer- and non-integer-indexed Bragg peaks, and the temperature dependence of these two sets is different. As expected, a similar behavior is observed in our single-crystal neutron diffraction results, as may be seen in Fig. 5.

In order to refine the magnetic structure at the lowest measured temperature we subtracted data collected at 20 K from those collected at 1.7 K. Our refinement demonstrates that the measured intensities, shown in Fig. 6, may be described by a magnetic unit cell containing two magnetic moments of distinct magnitudes, one "short" and one "long," both oriented ferromagnetically along **c**. The temperature dependence of the superstructure peaks, shown in Fig. 5, occurs because the ratio of the magnitudes of these two moments changes as the temperature is lowered below T_C. The integer-index peaks depend on the sum of the two moments, whereas the noninteger peaks depend on the difference. Accordingly, the ratio is largest at $T \simeq 8$ K where the intensity of the noninteger peaks is a maximum. At lower temperatures, the intensity of the noninteger peaks decreases as the moments become more similar in magnitude.

The refined magnetic structure using our model is represented in Fig. 7 for each domain. The long and short ordered moments at 1.7 K are found to be $2.3(3)\mu_B$ and $1.3(3)\mu_B$, respectively.

The magnetic structure proposed here differs from that of Ref. [46]. First, we do not find evidence for an incommensurate magnetic propagation vector **k**, observed in their powder sample. Second, in our model the two different values of the Nd ordered moment correlate directly with the two different crystal-field environments caused by the Pd/Si superstructure, which is not the case for the model of Ref. [46] as it assumes no superstructure. In fact, both models give the same diffraction intensities after domain averaging, but our model has a more physical basis with respect to the full crystallographic structure determined here.

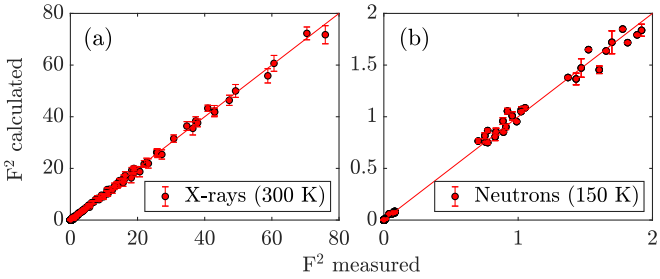


FIG. 4. Refinement results of the single-crystal diffraction measured with (a) x-rays at room temperature and (b) neutrons on D10+ at 150 K.

IV. INELASTIC NEUTRON SCATTERING

The conventional unit cell of the Nd_2PdSi_3 superstructure contains a total of 32 Nd atoms divided equally among two inequivalent Nd sites. Both sites have point-group symmetry C_2, but one is twofold and the other fourfold coordinated by Pd [see Fig. 8(a)]. Hence, the crystalline-electric field (CF) is expected to be different at these two sites. We note that, from the diffraction experiment alone, it is impossible to know whether the magnetic moments of the fourfold Pd-coordinated atoms are long and those of the twofold Pd-coordinated atoms are short, or vice versa.

Assuming that the Nd atoms adopt the usual 3+ valence, their LS-coupling $J = 9/2$ ground-state multiplet is split by the monoclinic CF into five Kramers doublets in

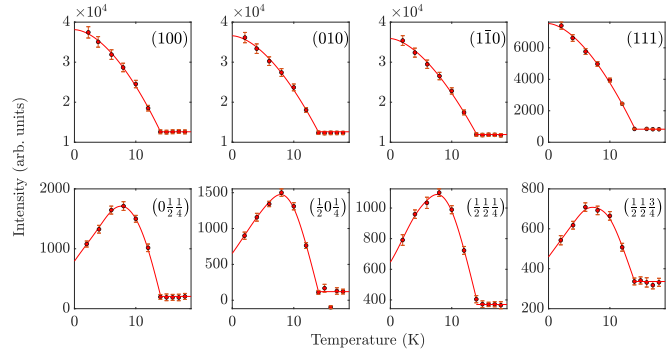


FIG. 5. Temperature dependence of Bragg-peak intensities for parent structure and superstructure reflections. For clarity, the indexing follows the hexagonal $P6/mmm$ space group description. Red lines are a guide to the eye.

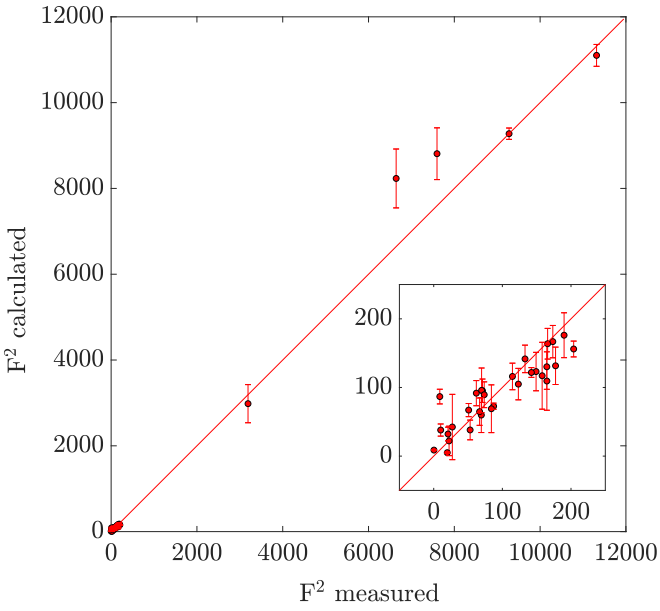


FIG. 6. Magnetic scattering measured on D10+. The inset shows the refinement of the weak reflections, associated mostly with the superstructure peaks.

the paramagnetic state. Below $T_C = 14$–17 K, when the compound develops a collinear ferromagnetic long-range order [31,34,37,46,52,54,55], each doublet is further split into two singlets by the exchange field. For two sites, a maximum of $2 \times (10 - 1) = 18$ excited levels form the magnetic spectrum at sufficiently low temperatures.

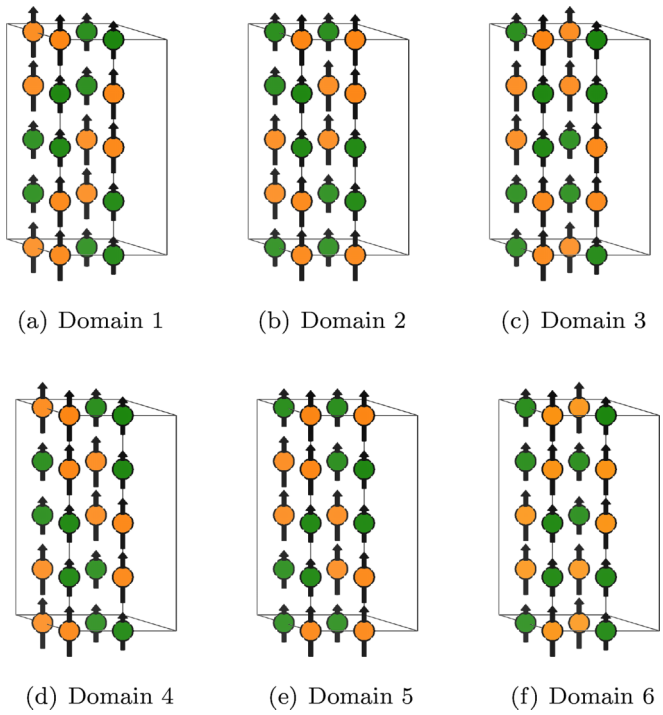


FIG. 7. (a)–(f) Magnetic structure of the six domains of Nd_2PdSi_3. In our unit-cell origin choice, orange atoms have long, while green have short magnetic moments.

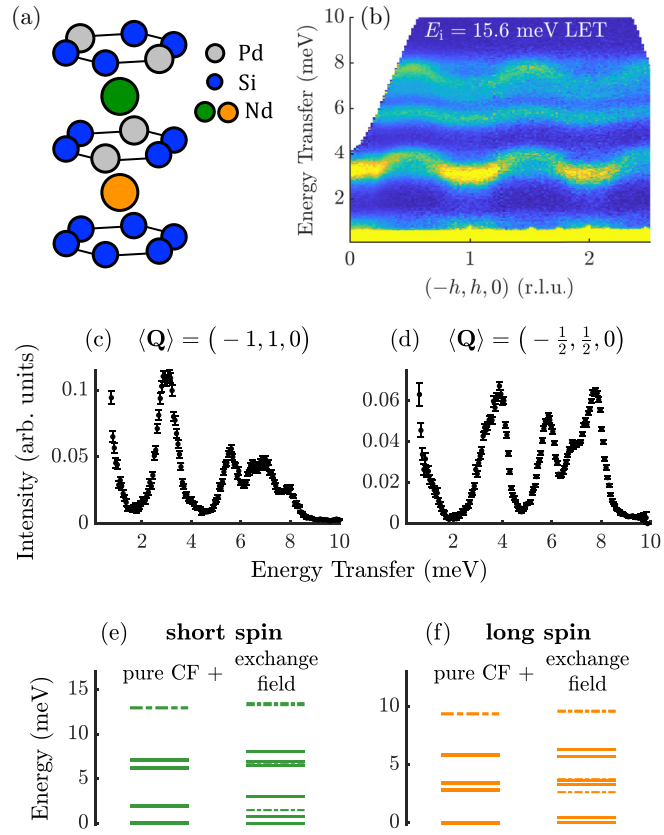


FIG. 8. (a) Part of the crystal structure of Nd_2PdSi_3, showing the local environments of the two Nd sites. Nd atoms (green/orange) may be fourfold coordinated (top) or twofold coordinated (bottom) by Pd atoms. (b) Inelastic neutron scattering spectrum measured on LET along $(-h, h, 0)$ at 1.7 K with neutrons of incident energy $E_i = 15.6$ meV. (c),(d) Constant-$\mathbf{Q}$ cuts performed at $\langle \mathbf{Q} \rangle = (-1, 1, 0)$ and $(-\frac{1}{2}, \frac{1}{2}, 0)$ reciprocal lattice units (r.l.u.), respectively. Data were integrated over ± 0.15 r.l.u. along $\langle \mathbf{Q} \rangle$ and two perpendicular directions. (e),(f) Nd CF levels for (e) short-spin and (f) long-spin sites, according to our model. Continuous and dashed lines represent, respectively, levels with nonzero or zero INS cross sections for excitation from the ground state.

Figure 8(b) shows the INS spectrum measured at a temperature of 1.7 K along the hexagonal reciprocal space direction $(-h, h, 0)$ and Figs. 8(c) and 8(d) are constant wave-vector $\mathbf{Q}$ cuts performed for $h = 1$ and $h = \frac{1}{2}$. Several dispersive modes, originating from the CF levels of the two inequivalent Nd sites, can be observed in the energy range from 2 to 8 meV. Higher resolution data (see below) confirm that there are in fact three levels with measurable intensity at energies between 2.7 and 4 meV, and another below 1 meV. Consistent with Ref. [46], no modes were observed above 8 meV, which implies that the spectrum manifest in Fig. 8(b) represents the entire observable $J = 9/2$ multiplet splitting of the Nd ions.

To model the data we used the mean-field random-phase approximation [56,57], which combines a description of the single-ion and two-ion interactions in a self-consistent way. The magnetic Hamiltonian is thus composed of two parts:

$$\mathcal{H} = \sum_i \mathcal{H}_i^{\mathrm{CF}} - \sum_{\langle ij \rangle} \mathbf{J}_i^{\mathrm{T}} \cdot \mathcal{J}_{ij} \cdot \mathbf{J}_j, \qquad (1)$$

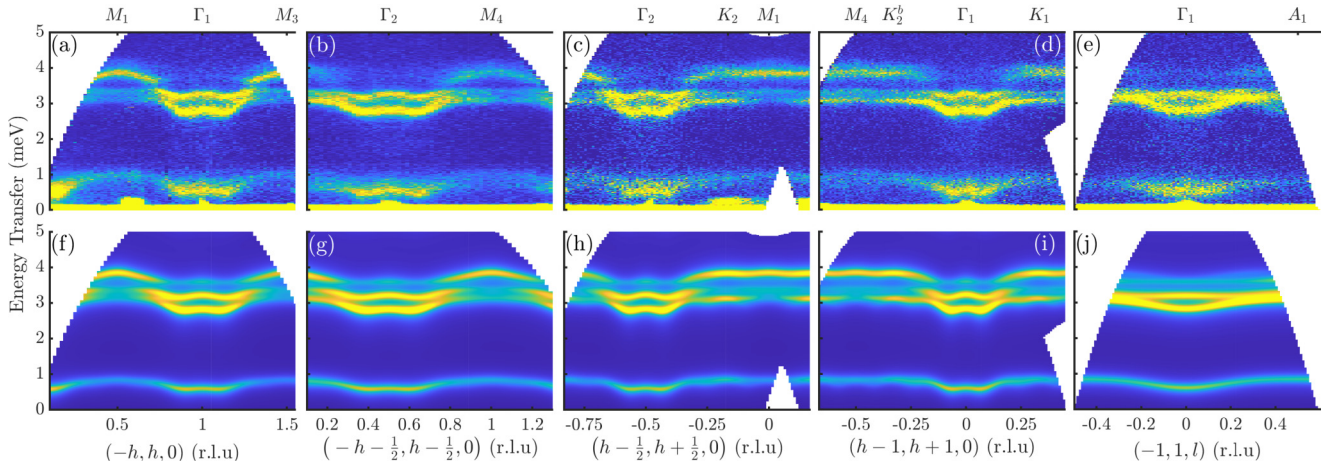


FIG. 9. (a)–(e) Spectra along several high-symmetry directions in reciprocal space measured on LET with neutrons of incident energy $E_i = 6$ meV, at a temperature of 1.7 K. Brillouin zone high-symmetry labels are shown above the panels, as defined in [52]. (f)–(j) Simulated spectra for the model that best describes the data displayed in (a)–(e). Positions in reciprocal space are indexed with respect to the parent $P6/mmm$ space group.

where $\mathcal{H}^{\mathrm{CF}}$ is the crystal-field component and $\mathcal{J}_{ij}$ are exchange matrices representing the (anisotropic) coupling between total angular momenta $\mathbf{J}_i$ and $\mathbf{J}_j$. We consider the approximate CF Hamiltonian

$$\mathcal{H}^{\mathrm{CF}} = \sum_{k=2,4,6} B_0^k \hat{C}_0^{(k)} + B_6^6 \left(\hat{C}_6^{(6)} + \hat{C}_{-6}^{(6)}\right), \tag{2}$$

where $\hat{C}_{\pm q}^{(k)}$ are Wybourne tensor operators and B_q^k the corresponding parameters. The site subscript is omitted here for simplicity. The Hamiltonian in Eq. (2) describes the leading-order $6/mmm$ point symmetry at the Nd site of the hexagonal parent structure. Although the true point symmetry requires more parameters, the truncated Hamiltonian (2) already fully splits the $J = 9/2$ manifold. The higher-order terms do not cause any further loss of degeneracy, so their effects can be approximately absorbed into the four parameters included in Eq. (2) and in the exchange Hamiltonian developed below.

We find that a satisfactory fit can be achieved as long as a consistent assignment of levels is made to each one of the two Nd sites. Data collected in magnetic fields up to 11 T applied along **c** were used to constrain the CF model [52]. Figures 8(e) and 8(f) present the crystal-field scheme that best reproduces the observed excitations. Because $\mathcal{H}^{\mathrm{CF}}$ differs for both sites, the ground-state magnetic moments for the two Nd are distinct. The Nd with the lowest (highest) ground-state magnetic moment is referred to as *short spin* (*long spin*) [see Figs. 8(e) and 8(f)]. The B_q^k parameters found in this work are listed in [52].

The determination of the exchange couplings was made using higher-resolution INS data shown in Figs. 9(a)–9(e), which provide a detailed view of the excitations up to 5 meV. Three levels can be resolved between 2 and 4 meV—two of the modes soften at the Γ point and, separated by a small gap, a third mode disperses to higher energies ∼4 meV towards the M points. We identify these modes as three different CF levels. According to our model, the mode of lowest energy out of the trio belongs to the short-spin site, while the upper two belong to the long-spin site [see Figs. 8(e) and 8(f)]. The level below 1 meV originates from the splitting of the doublet ground state on the short-spin sites. Although the ground state of the long-spin site also splits by ∼1 meV, this transition has very small scattering intensity and cannot be observed in the data.

From the general softening of the modes near the Γ point [see Figs. 9(a)–9(d)], it can be inferred that the dominant nearest-neighbor in-plane couplings are ferromagnetic, which agrees with the magnetic structure reported in Ref. [46] and also with our own neutron diffraction data. A striking additional feature of the in-plane dispersion is a high-frequency modulation that has a local maximum at Γ. The periodicity of the oscillations, which is slightly different for the modes originating from each of the Nd sites, implies that higher-neighbor antiferromagnetic interactions are significant. We find that the closest in-plane antiferromagnetic coupling is between fifth-nearest neighbors, i.e., third-nearest neighbors within the *ab* plane [52].

The simulated spectra shown in Figs. 9(f)–9(j) are from the best model we could find to describe the data, taking into account the six possible superstructure domains [52]. The simulations reproduce all the main observed features. Figure 10(a) plots the model exchange parameters as represented by the trace of the exchange matrices as a function of the nth-neighbor distance r_n. The exchange interactions are seen to extend to large distances and tend to oscillate with r_n. With two distinct Nd sites in the superstructure, symmetry-inequivalent exchange couplings cannot be discriminated simply by bond distance. Because of that, the $\mathcal{J}_{ij}$ in Fig. 10(a) are labeled with a superscript—long-long (ll), short-short (ss), or long-short (ls)—indicating which sites are coupling, and a subscript n for bonds at a distance r_n. These are illustrated in the inset of Fig. 10(a) for first and second neighbors. A complete symmetry analysis of the couplings and the assumptions made in this work can be found in the Supplemental Material [52]. Figure 10(b) shows the Fourier transform $\mathcal{J}(\mathbf{Q})$ of the in-plane exchange interactions calculated for each Nd site from the values of $\mathrm{Tr}\{\mathcal{J}_n\}$. The maximum in $\mathcal{J}(\mathbf{Q})$ is found at the hexagonal reciprocal lattice

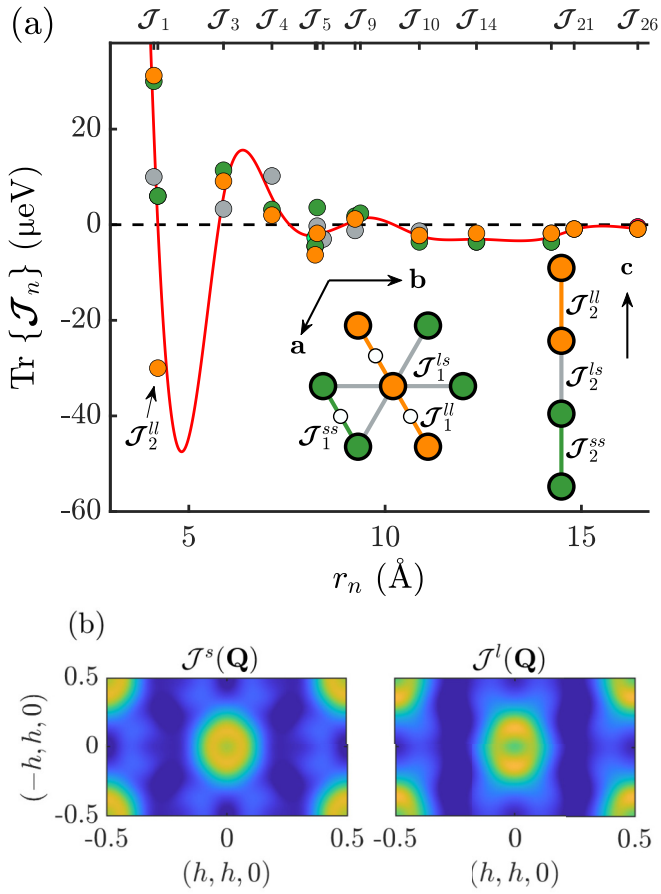


FIG. 10. (a) Trace of the exchange-coupling matrices used to obtain the spectra in Fig. 9, as a function of nth-neighbor distance r_n. Colors orange, gray, and green correspond to ll, ls, and ss couplings, respectively. The continuous line is a guide to the eye. Insets show first- and second-nearest-neighbor exchange pathways, $\mathcal{J}_1$ and $\mathcal{J}_2$. Open circles indicate positions of inversion centers. (b) In-plane variation of the Fourier transform of Tr$\{\mathcal{J}_n\}$ for each Nd site. Note: in hexagonal geometry the direction $(-h, h, 0)$ is equivalent to $(h, 0, 0)$.

vector $\mathbf{Q}_\mathrm{m} = (q, 0, 0)$, where $q \simeq 0.12/0.14$ for the s/l sites, respectively.

Figure 9(e), which shows the out-of-plane dispersion measured along $(-1, 1, l)$, reveals something else about the exchange interactions. The modes originating from the short-spin sites (centered on ∼0.8 and 3 meV) are seen to soften by about 0.4 meV at the Γ_1 point, whereas the modes associated with the long-spin sites (3.3 and 3.6 meV) are essentially dispersionless. The observation of flat modes suggests that the magnetic coupling between the long-spin sites is highly frustrated. Consistent with this, our model finds the nearest-neighbor in-plane and out-of-plane couplings between long spins to be similar in magnitude but opposite in sign, as can be seen from the points (orange symbols) in Fig. 10(a) representing $\mathcal{J}_1^{ll}$ and $\mathcal{J}_2^{ll}$. By contrast, we find no significant short-range frustration within the Nd layers, e.g., the $\mathcal{J}_5$ and $\mathcal{J}_1$ couplings also have opposite sign but differ by an order of magnitude.

Our simplifying assumption of sixfold rotational symmetry for $\mathcal{H}^\mathrm{CF}$, Eq. (2), constrains the single-ion anisotropy to be isotropic in the ab plane. The true $Fddd$ symmetry, however,

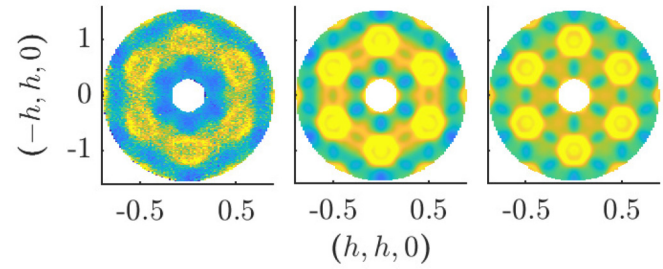


FIG. 11. Constant-energy slices through data (left) and models (middle and right) integrated over the energy interval 3.0–3.3 meV. The 360° data map was constructed by rotation of a measured 120° sector. Middle panel shows simulations using anisotropic exchange coupling, as in Figs. 9(f)–9(j). Right panel is for an isotropic exchange model.

allows in-plane single-ion anisotropy as well as anisotropic $\mathcal{J}_{ij}$ couplings along most paths [52]. Although not apparent in Fig. 9, the effects of magnetic anisotropy can be seen in the constant-energy maps of Fig. 11, which integrate over the middle of the three bands located between 3 and 4 meV. The data (left panel) display twofold symmetry around the reciprocal lattice points, whereas the intensity calculated from a model with isotropic exchange interactions (right panel) has sixfold symmetry. The main features of the data are reproduced reasonably well by our model with anisotropic exchange interactions (middle panel). The intensity map has sixfold symmetry around the origin because of the averaging of the six twofold symmetric domains. We stress that anisotropy in the spectrum could also arise from higher-order terms in $\mathcal{H}^\mathrm{CF}$, but the effects of single- and two-ion anisotropy are very difficult to separate.

V. DISCUSSION AND CONCLUSIONS

Our model has a large parameter set, and there may exist other sets that give similar agreement. However, by exploring the effects of varying the parameters we have found that the general features summarized above are robust. Moreover, there are good reasons to expect that our overall findings will extend to the SkX compound Gd_2PdSi_3. First, the superstructures of the Nd and Gd compounds are essentially the same (the only difference being a doubling along the c axis in the latter). Second, our first-principles calculations (see Fig. 12

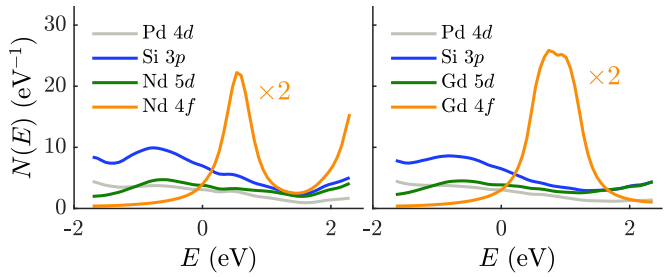


FIG. 12. Calculated density of states for selected bands close to the Fermi energy ($E = 0$ eV) for Nd_2PdSi_3 (left) and Gd_2PdSi_3 (right). The Nd_2PdSi_3 superstructure is assumed in both cases. The 4f bands have been scaled down by a factor of 2.

and Supplemental Material [52]), as well as experimental studies [58], indicate that the electronic structure near the Fermi energy in R_2PdSi_3 does not vary significantly with R. In particular, the $5d$ bands, which are believed to be important for skyrmion formation [18], are very similar in the two compounds (Fig. 12). Third, the $\mathcal{J}(\mathbf{Q})$ for Nd_2PdSi_3, Fig. 10(b), is maximal at a wave vector with the same direction and similar magnitude ($q = 0.12$–0.14) as the observed zero-field magnetic propagation vector of Gd_2PdSi_3 ($q \simeq 0.14$) [25]. This implies that the magnetic interactions in the Nd and Gd compounds are similar. Incommensurate in-plane magnetic order does not occur in the Nd case because the crystal-field anisotropy locks the Nd moments along the c axis and drives ferromagnetic order.

Consequently, our comprehensive study of the magnetic spectrum of single-crystal Nd_2PdSi_3 has important implications for the formation of a SkX phase in Gd_2PdSi_3. Our data reveal a critical dependence on the Pd/Si superstructure, such that the pattern of magnetic interactions has orthorhombic, not hexagonal symmetry. Our results also raise questions about the role played by geometric frustration in the magnetism displayed by this family of compounds. Although there are some frustrated magnetic interactions, especially associated with the antiferromagnetic $\mathcal{J}_2^{ll}$ nearest-neighbor coupling along the c axis, we do not find evidence for strong short-range frustration within the Nd layers. Our analysis, moreover, has revealed the long-range nature of the magnetic interactions, with non-negligible couplings extending up to at least the 26th nearest neighbor and a tendency to oscillate with distance. The evidence presented here suggests that theories for the SkX phase in Gd_2PdSi_3 must go beyond simple models of short-range frustrated interactions on a triangular lattice, and point instead towards approaches based on longer-range RKKY exchange. Such considerations may also apply to other metallic centrosymmetric SkX materials.

ACKNOWLEDGMENTS

The research at Oxford was supported by UK Research and Innovation, Grant No. EP/T027991/1, and by the Oxford–ShanghaiTech collaboration project. The work at Warwick was supported by UK Research and Innovation, Grants No. EP/T005963/1 and No. EP/N032128/1. J.B. was supported by the Alexander von Humboldt Foundation through the Feodor Lynen Research Fellowship for Postdocs. Data from the neutron experiments are available from the STFC ISIS Neutron and Muon Source, Proposals No. RB2010616 (Merlin [59]), No. RB2000180 (Merlin [60]), and No. RB2310234 (LET [61]), and from the Institut Laue-Langevin, Proposal No. 5-41-1185 (D3 [62]).

DATA AVAILABILITY

The data that support the findings of this article are openly available [53,54,55], embargo periods may apply.

[1] S. Mühlbauer, B. Binz, F. Jonietz, C. Pfleiderer, A. Rosch, A. Neubauer, R. Georgii, and P. Böni, Skyrmion lattice in a chiral magnet, Science **323**, 915 (2009).

[2] C. Pappas, E. Lelièvre-Berna, P. Falus, P. M. Bentley, E. Moskvin, S. Grigoriev, P. Fouquet, and B. Farago, Chiral paramagnetic skyrmion-like phase in MnSi, Phys. Rev. Lett. **102**, 197202 (2009).

[3] X. Z. Yu, Y. Onose, N. Kanazawa, J. H. Park, J. H. Han, Y. Matsui, N. Nagaosa, and Y. Tokura, Real-space observation of a two-dimensional skyrmion crystal, Nature (London) **465**, 901 (2010).

[4] A. Fert, V. Cros, and J. Sampaio, Skyrmions on the track, Nat. Nanotechnol. **8**, 152 (2013).

[5] T. Lancaster, Skyrmions in magnetic materials, Contemp. Phys. **60**, 246 (2019).

[6] A. N. Bogdanov and C. Panagopoulos, Physical foundations and basic properties of magnetic skyrmions, Nat. Rev. Phys. **2**, 492 (2020).

[7] L. Thomas, F. Lionti, R. Ballou, D. Gatteschi, R. Sessoli, and B. Barbara, Macroscopic quantum tunnelling of magnetization in a single crystal of nanomagnets, Nature (London) **383**, 145 (1996).

[8] R. Wiesendanger, Nanoscale magnetic skyrmions in metallic films and multilayers: A new twist for spintronics, Nat. Rev. Mater. **1**, 16044 (2016).

[9] C. Moreau-Luchaire, C. Moutafis, N. Reyren, J. Sampaio, C. A. F. Vaz, N. Van Horne, K. Bouzehouane, K. Garcia, C. Deranlot, P. Warnicke, P. Wohlhüter, J. M. George, M. Weigand, J. Raabe, V. Cros, and A. Fert, Additive interfacial chiral interaction in multilayers for stabilization of small individual skyrmions at room temperature, Nat. Nanotechnol. **11**, 444 (2016).

[10] C. Psaroudaki and C. Panagopoulos, Skyrmion qubits: A new class of quantum logic elements based on nanoscale magnetization, Phys. Rev. Lett. **127**, 067201 (2021).

[11] J. Xia, X. Zhang, X. Liu, Y. Zhou, and M. Ezawa, Universal quantum computation based on nanoscale skyrmion helicity qubits in frustrated magnets, Phys. Rev. Lett. **130**, 106701 (2023).

[12] T. Okubo, S. Chung, and H. Kawamura, Multiple-q states and the skyrmion lattice of the triangular-lattice Heisenberg antiferromagnet under magnetic fields, Phys. Rev. Lett. **108**, 017206 (2012).

[13] A. O. Leonov and M. Mostovoy, Multiply periodic states and isolated skyrmions in an anisotropic frustrated magnet, Nat. Commun. **6**, 8275 (2015).

[14] V. Lohani, C. Hickey, J. Masell, and A. Rosch, Quantum skyrmions in frustrated ferromagnets, Phys. Rev. X **9**, 041063 (2019).

[15] Z. Wang, Y. Su, S.-Z. Lin, and C. D. Batista, Skyrmion crystal from RKKY interaction mediated by 2D electron gas, Phys. Rev. Lett. **124**, 207201 (2020).

[16] Z. Wang, Y. Su, S.-Z. Lin, and C. D. Batista, Meron, skyrmion, and vortex crystals in centrosymmetric tetragonal magnets, Phys. Rev. B **103**, 104408 (2021).

[17] S. Hayami, R. Ozawa, and Y. Motome, Effective bilinear-biquadratic model for noncoplanar ordering in itinerant magnets, Phys. Rev. B **95**, 224424 (2017).

[18] T. Nomoto, T. Koretsune, and R. Arita, Formation mechanism of the helical $\boldsymbol{Q}$ structure in Gd-based skyrmion materials, Phys. Rev. Lett. **125**, 117204 (2020).

[19] S.-Z. Lin and S. Hayami, Ginzburg–Landau theory for skyrmions in inversion-symmetric magnets with competing interactions, Phys. Rev. B **93**, 064430 (2016).

[20] O. I. Utesov, Mean-field description of skyrmion lattice in hexagonal frustrated antiferromagnets, Phys. Rev. B **105**, 054435 (2022).

[21] S. Hayami and Y. Motome, Square skyrmion crystal in centrosymmetric itinerant magnets, Phys. Rev. B **103**, 024439 (2021).

[22] K. Mitsumoto and H. Kawamura, Replica symmetry breaking in the RKKY skyrmion-crystal system, Phys. Rev. B **104**, 184432 (2021).

[23] J. Bouaziz, E. Mendive-Tapia, S. Blügel, and J. B. Staunton, Fermi-surface origin of skyrmion lattices in centrosymmetric rare-earth intermetallics, Phys. Rev. Lett. **128**, 157206 (2022).

[24] Y. Dong, Y. Arai, K. Kuroda, M. Ochi, N. Tanaka, Y. Wan, M. D. Watson, T. K. Kim, C. Cacho, M. Hashimoto, D. Lu, Y. Aoki, T. D. Matsuda, and T. Kondo, Fermi surface nesting driving the RKKY interaction in the centrosymmetric skyrmion magnet Gd_2PdSi_3, Phys. Rev. Lett. **133**, 016401 (2024).

[25] T. Kurumaji, T. Nakajima, M. Hirschberger, A. Kikkawa, Y. Yamasaki, H. Sagayama, H. Nakao, Y. Taguchi, T. Arima, and Y. Tokura, Skyrmion lattice with a giant topological Hall effect in a frustrated triangular-lattice magnet, Science **365**, 914 (2019).

[26] M. Hirschberger, T. Nakajima, S. Gao, L. Peng, A. Kikkawa, T. Kurumaji, M. Kriener, Y. Yamasaki, H. Sagayama, H. Nakao, K. Ohishi, K. Kakurai, Y. Taguchi, X. Yu, T.-h. Arima, and Y. Tokura, Skyrmion phase and competing magnetic orders on a breathing kagomé lattice, Nat. Commun. **10**, 5831 (2019).

[27] N. D. Khanh, T. Nakajima, X. Yu, S. Gao, K. Shibata, M. Hirschberger, Y. Yamasaki, H. Sagayama, H. Nakao, L. Peng, K. Nakajima, R. Takagi, T.-h. Arima, Y. Tokura, and S. Seki, Nanometric square skyrmion lattice in a centrosymmetric tetragonal magnet, Nat. Nanotechnol. **15**, 444 (2020).

[28] R. Takagi, N. Matsuyama, V. Ukleev, L. Yu, J. S. White, S. Francoual, J. R. L. Mardegan, S. Hayami, H. Saito, K. Kaneko, K. Ohishi, Y. Ōnuki, A. Taka-Hisa, Y. Tokura, T. Nakajima, and S. Seki, Square and rhombic lattices of magnetic skyrmions in a centrosymmetric binary compound, Nat. Commun. **13**, 1472 (2022).

[29] S. Gao, H. D. Rosales, F. A. G. Albarracín, V. Tsurkan, G. Kaur, T. Fennell, P. Steffens, M. Boehm, P. Čermák, A. Schneidewind, E. Ressouche, D. C. Cabra, C. Rüegg, and O. Zaharko, Fractional antiferromagnetic skyrmion lattice induced by anisotropic couplings, Nature (London) **586**, 37 (2020).

[30] R. Mallik, E. V. Sampathkumaran, M. Strecker, and G. Wortmann, Observation of a minimum in the temperature-dependent electrical resistance above the magnetic-ordering temperature in Gd_2PdSi_3, Europhys. Lett. **41**, 315 (1998).

[31] P. Kotsanidis, J. Yakinthos, and E. Gamari-Seale, Magnetic properties of the ternary rare earth silicides R_2PdSi_3 (R=Pr, Nd, Gd, Tb, Dy, Ho, Er, Tm and Y), J. Magn. Magn. Mater. **87**, 199 (1990).

[32] R. Mallik, E. Sampathkumaran, and P. Paulose, Large low temperature magnetoresistance and magnetic anomalies in Tb_2PdSi_3 and Dy_2PdSi_3, Solid State Commun. **106**, 169 (1998).

[33] S. R. Saha, H. Sugawara, T. D. Matsuda, Y. Aoki, H. Sato, and E. V. Sampathkumaran, Magnetic, thermal, and transport properties of single crystals of antiferromagnetic Kondo-lattice Ce_2PdSi_3, Phys. Rev. B **62**, 425 (2000).

[34] A. Szytuła, M. Hofmann, B. Penc, M. Ślaski, S. Majumdar, E. Sampathkumaran, and A. Zygmunt, Magnetic behaviour of R_2PdSi_3 compounds with R=Ce, Nd, Tb–Er, J. Magn. Magn. Mater. **202**, 365 (1999).

[35] M. Frontzek, A. Kreyssig, M. Doerr, A. Schneidewind, J.-U. Hoffmann, and M. Loewenhaupt, Frustration in R_2PdSi_3 (R=Tb, Er) compounds: Spin-glass or magnetic short range order? Neutron diffraction studies, J. Phys.: Condens. Matter **19**, 145276 (2007).

[36] M. Frontzek, A. Kreyssig, M. Doerr, M. Rotter, G. Behr, W. Löser, I. Mazilu, and M. Loewenhaupt, Magneto-crystalline anisotropy in R_2PdSi_3 (R=Tb, Dy, Ho, Er, Tm) single crystals, J. Magn. Magn. Mater. **301**, 398 (2006).

[37] D. X. Li, S. Nimori, Y. Shiokawa, Y. Haga, E. Yamamoto, and Y. Onuki, ac susceptibility and magnetic relaxation of R_2PdSi_3 (R = Nd, Tb, and Dy), Phys. Rev. B **68**, 012413 (2003).

[38] S. Majumdar, E. V. Sampathkumaran, P. L. Paulose, H. Bitterlich, W. Löser, and G. Behr, Anisotropic giant magnetoresistance, magnetocaloric effect, and magnetic anomalies in single crystalline Tb_2PdSi_3, Phys. Rev. B **62**, 14207 (2000).

[39] S. Majumdar, H. Bitterlich, G. Behr, W. Löser, P. L. Paulose, and E. V. Sampathkumaran, Magnetic and transport behavior of single-crystalline Dy_2PdSi_3, Phys. Rev. B **64**, 012418 (2001).

[40] P. L. Paulose, E. V. Sampathkumaran, H. Bitterlich, G. Behr, and W. Löser, Anisotropic spin-glass-like and quasi-one-dimensional magnetic behavior in the intermetallic compound Tb_2PdSi_3, Phys. Rev. B **67**, 212401 (2003).

[41] S. R. Saha, H. Sugawara, T. D. Matsuda, H. Sato, R. Mallik, and E. V. Sampathkumaran, Magnetic anisotropy, first-order-like metamagnetic transitions, and large negative magnetoresistance in single-crystal Gd_2PdSi_3, Phys. Rev. B **60**, 12162 (1999).

[42] M. Gomilšek, T. J. Hicken, M. N. Wilson, K. J. A. Franke, B. M. Huddart, A. Štefančič, S. J. R. Holt, G. Balakrishnan, D. A. Mayoh, M. T. Birch, S. H. Moody, H. Luetkens, Z. Guguchia, M. T. F. Telling, P. J. Baker, S. J. Clark, and T. Lancaster, Anisotropic skyrmion and multi-q spin dynamics in centrosymmetric Gd_2PdSi_3, Phys. Rev. Lett. **134**, 046702 (2025).

[43] J. A. M. Paddison, B. K. Rai, A. F. May, S. Calder, M. B. Stone, M. D. Frontzek, and A. D. Christianson, Magnetic interactions of the centrosymmetric skyrmion material Gd_2PdSi_3, Phys. Rev. Lett. **129**, 137202 (2022).

[44] J. Ju, H. Saito, T. Kurumaji, M. Hirschberger, A. Kikkawa, Y. Taguchi, T. H. Arima, Y. Tokura, and T. Nakajima, Polarized neutron scattering study of the centrosymmetric skyrmion host material Gd_2PdSi_3, Phys. Rev. B **107**, 024405 (2023).

[45] D. Mayoh, A. Štefančič, M. Lees, and G. Balakrishnan, Crystal growth of the R_2PdSi_3 (R=rare earth) materials using the optical floating zone technique, J. Cryst. Growth **642**, 127774 (2024).

[46] M. Smidman, C. Ritter, D. T. Adroja, S. Rayaprol, T. Basu, E. V. Sampathkumaran, and A. D. Hillier, Magnetic order in Nd_2PdSi_3 investigated using neutron scattering and muon spin relaxation, Phys. Rev. B **100**, 134423 (2019).

[47] R. I. Bewley, R. S. Eccleston, K. A. McEwen, S. M. Hayden, M. T. Dove, S. M. Bennington, J. R. Treadgold, and R. L. S. Coleman,, MERLIN: A new high count rate spectrometer at ISIS, Phys. B: Condens. Matter **385**, 1029 (2006).

[48] R. Bewley, J. Taylor, and S. Bennington, LET, a cold neutron multi-disk chopper spectrometer at ISIS, Nucl. Instrum. Methods Phys. Res. Sect. A **637**, 128 (2011).

[49] J. Lass *et al.*, Commissioning of the novel continuous angle multi-energy analysis spectrometer at the Paul Scherrer Institut, Rev. Sci. Instrum. **94**, 023302 (2023).

[50] J. Lass, H. Jacobsen, D. G. Mazzone, and K. Lefmann, MJOLNIR: A software package for multiplexing neutron spectrometers, SoftwareX **12**, 100600 (2020).

[51] F. Tang, M. Frontzek, J. Dshemuchadse, T. Leisegang, M. Zschornak, R. Mietrach, J.-U. Hoffmann, W. Löser, S. Gemming, D. C. Meyer, and M. Loewenhaupt, Crystallographic superstructure in R_2PdSi_3 compounds (R = heavy rare earth), Phys. Rev. B **84**, 104105 (2011).

[52] See Supplemental Material at http://link.aps.org/supplemental/10.1103/vpy4-9zgh for details of the sample characterization, x-ray and neutron diffraction data of the Pd/Si superstructure and magnetic structure, data analysis, model, *ab initio* electronic structure calculations, and for additional figures showing fits to the data, which includes Refs. [23,63–66].

[53] J. Rodríguez-Carvajal, Recent advances in magnetic structure determination by neutron powder diffraction, Phys. B (Amsterdam, Neth.) **192**, 55 (1993).

[54] Y. Xu, W. Löser, F. Tang, C. G. F. Blum, L. Liu, and B. Büchner, Crystal growth of the intermetallic compound Nd_2PdSi_3, Cryst. Res. Technol. **46**, 135 (2011).

[55] K. Mukherjee, T. Basu, K. K. Iyer, and E. V. Sampathkumaran, $4f$ hybridization effect on the magnetism of Nd_2PdSi_3, Phys. Rev. B **84**, 184415 (2011).

[56] J. Jensen and A. R. Mackintosh, *Rare Earth Magnetism* (Clarendon Press, Oxford, 1991).

[57] A. T. Boothroyd, *Principles of Neutron Scattering from Condensed Matter* (Oxford University Press, Oxford, UK, 2020).

[58] D. S. Inosov, D. V. Evtushinsky, A. Koitzsch, V. B. Zabolotnyy, S. V. Borisenko, A. A. Kordyuk, M. Frontzek, M. Loewenhaupt, W. Löser, I. Mazilu, H. Bitterlich, G. Behr, J.-U. Hoffmann, R. Follath, and B. Büchner, Electronic structure and nesting-driven enhancement of the RKKY interaction at the magnetic ordering propagation vector in Gd_2PdSi_3 and Tb_2PdSi_3, Phys. Rev. Lett. **102**, 046401 (2009).

[59] M. Smidman, G. Balakrishnan, D. Le, D. Mayoh, E. V. Sampathkumaran, D. T. Adroja, Z. Shan, and V. Peçanha-Antonio, Spin-waves in Nd_2PdSi_3 with coexistent ferromagnetism and antiferromagnetism, STFC ISIS Neutron and Muon Source (2020), https://doi.org/10.5286/ISIS.E.RB2010616.

[60] M. Smidman, D. Le, D. Mayoh, D. T. Adroja, G. Balakrishnan, and Z. Shan, Spin-waves in Nd_2PdSi_3 with coexistent ferromagnetism and antiferromagnetism, STFC ISIS Neutron and Muon Source (2020), https://doi.org/10.5286/ISIS.E.RB2000180.

[61] V. Peçanha-Antonio, C. Balz, D. T. Adroja, Z. Shan, M. Smidman, and A. T. Boothroyd, Magnetic excitons in the frustrated topological Nd_2PdSi_3, STFC ISIS Neutron and Muon Source (2023), https://doi.org/10.5286/ISIS.E.RB2310234.

[62] V. Peçanha-Antonio, D. T. Adroja, N. A. Katcho, A. T. Boothroyd, B. Ouladdiaf, and M. Smidman, Magnetic structure of the frustrated, triangular-lattice metallic magnet Nd_2PdSi_3, Institut Laue-Langevin (ILL) (2023), https://doi.ill.fr/10.5291/ILL-DATA.5-41-1185.

[63] C. E. Patrick and J. B. Staunton, MARMOT: Magnetism, anisotropy, and more, using the relativistic disordered local moment picture at finite temperature, Electron. Struct. **4**, 017001 (2022).

[64] M. Lüders, A. Ernst, M. Däne, Z. Szotek, A. Svane, D. Ködderitzsch, W. Hergert, B. L. Györffy, and W. M. Temmerman, Self-interaction correction in multiple scattering theory, Phys. Rev. B **71**, 205109 (2005).

[65] M. Hoffmann, A. Ernst, W. Hergert, V. N. Antonov, W. A. Adeagbo, R. M. Geilhufe, and H. Ben Hamed, Magnetic and electronic properties of complex oxides from first-principles, Phys. Status Solidi B **257**, 1900671 (2020).

[66] J. Bouaziz, G. Bihlmayer, C. E. Patrick, J. B. Staunton, and S. Blügel, Origin of incommensurate magnetic order in the *R*AlSi magnetic Weyl semimetals (R = Pr, Nd, Sm), Phys. Rev. B **109**, L201108 (2024).